LANGMUIR

pubs.acs.org/Langmuir Article

Reversal of Electroosmotic Flow in Charged Nanopores with Multivalent Electrolyte

Igor M. Telles,* Yan Levin,* and Alexandre P. dos Santos*

Cite This: *Langmuir* 2022, 38, 3817−3823 Read Online

ACCESS | Metrics & More | Article Recommendations

ABSTRACT: We study the reversal of electroosmotic flow in charged cylindrical nanopores containing multivalent electrolyte. Dissipative particle dynamics is used to simulate the hydrodynamics of the electroosmotic flow. The electrostatic interactions are treated using 3D Ewald summation, corrected for a pseudo-one-dimensional geometry of the pore. We observe that, for sufficiently large surface charge density, condensation of multivalent counterions leads to the reversal of the pore's surface charge. This results in the reversal of electroosmotic flow. Our simulations show that the Smoluchowski equation is able to quantitatively account for the electroosmotic flow through the nanopore, if the shear plane is shifted from the position of the Stern contact surface.

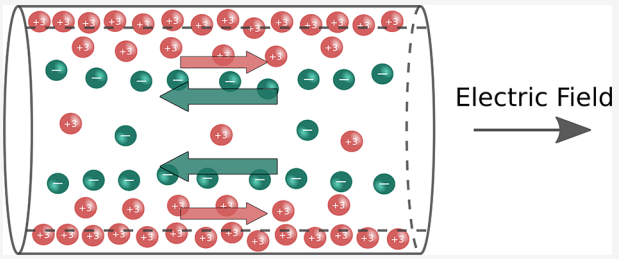

INTRODUCTION

Confined electrolyte solutions are important for electronics,[1,2] energy conversion,[3−5] and supercapacitors.[6,7] In many industrial[8,9] and life science applications,[10,11] one is often faced with the transport of electrolyte through nanopores.[12−14] A particularly important phenomenon is the flow of confined electrolyte solution under the action of an electric field.[15−17] This is known as electroosmotic flow (EOF). In this process, ionized solute particles, accelerated by the external electric field, transfer part of their momentum to the solvent, resulting in an overall fluid flow. The EOF has a huge span of applications ranging from chemistry[18−21] and biology[22−25] to applied[26,27] and geological[28,29] sciences. Numerous works have studied liquid transport at the micro- and nanoscale, making possible the development of microfluidic devices,[30−32] ionic circuits,[33] energy harvesting,[34,35] and identification of viral particles.[36] In spite of significant progress over the past several years, many challenges remain. While atomistic simulations are now practical for studying small ion channels imbedded into a cellular membranes, the simulation of fluid transport through long nanopores requires more coarse-grained simulation methods, such as the dissipative particle dynamics (DPD) or lattice Boltzmann simulations. Nevertheless, in recent years, there have been a number of attempts to use atomistic simulations to study EOF.[37−40] One challenge faced when trying to use atomistic simulations is the large system sizes necessary to tackle the hydrodynamic time and space scales. Furthermore, the force fields used in atomistic simulations have been optimized to study bulk properties, while the EOF is fundamentally a surface phenomenon. Thus, one needs an accurate force field that describes the interaction of ions with surfaces and surrounding water molecules. In a highly restrictive nanopore geometry, any imperfections in the force field can lead to erroneous conclusions. In view of these observations, in the present paper, we will use a coarse-grained DPD simulation method to explore more general issues unrelated to the specific model of water or ionic force fields. The questions that we will try to address are the following: Does the Smoluchowski equation remain valid inside cylindrical nanopores containing multivalent electrolyte? What is the location of the shear plane at which the fluid velocity vanishes? Is it possible to reverse EOF in strongly charged nanopores?

The reversal of the electrophoretic mobility is experimentally well-known for colloidal suspensions with multivalent counterions.[41−43] In addition to ionic correlations, the phenomenon is also affected by the surface chemistry, which can lead to specific adsorption of multivalent counterions.[44,45] Much less is known about EOF inside charged nanopores. In this work, we will use DPD simulations to account for the hydrodynamic flow inside charged cylindrical nanopores. The DPD is specifically constructed in such a way as to locally conserve the momentum as well as to satisfy the fluctuation−dissipation theorem, resulting in the correct hydrodynamic limit even for a relatively small number of particles.[46] To account for the long-range electrostatic interactions between ions, we will use a recently developed 3D Ewald summation method modified for the non-

Received: December 29, 2021
Revised: March 3, 2022
Published: March 16, 2022

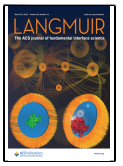

https://doi.org/10.1021/acs.langmuir.1c03475
Langmuir 2022, 38, 3817−3823

neutral pseudo-one-dimensional geometry of the pore's interior.[47]

MODEL AND SIMULATION DETAILS

Consider N_{sol} solvent particles and N charged particles, all with mass m, inside a cylinder of radius $R = 10l_B$, length $L_z = 10l_B$, and surface charge density σ, as shown in Figure 1. The ions have

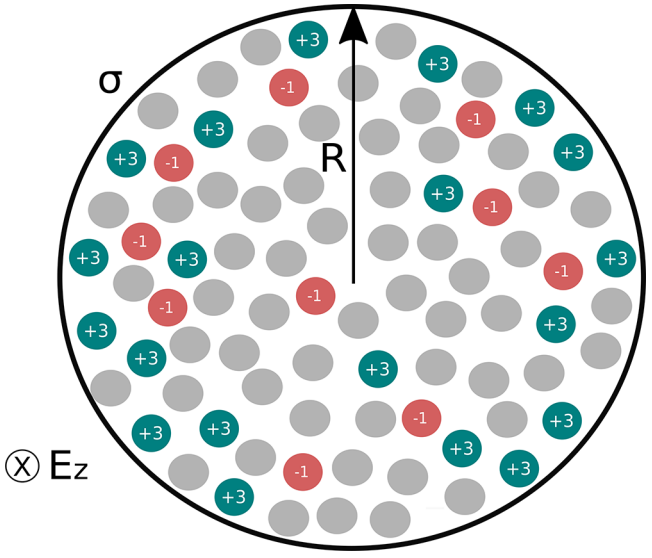

Figure 1. Schematic illustration of the simulated system. Solvent particles, trivalent counterions, and monovalent co-ions are confined in an infinite charged cylindrical pore of radius R and uniform surface charge density σ. The cylinder is oriented along the z axis. The electric field is applied in the $\hat{z}$ direction.

radius $r_i = 0.25l_B$. The natural length in our simulations is the Bjerrum length $l_B = q^2\beta/\epsilon$, where $\beta = 1/k_BT$. Its value is $l_B = 7.2$ Å for water at room temperature. In the present work, the dielectric constant ϵ is taken to be uniform over all space. However, It is possible to include the dielectric discontinuity across the pore surface into the formalism described below.[48] Periodic boundary conditions are implemented in the z direction, and the no-slip boundary condition at the ion contact surface, $\sqrt{x^2 + y^2} = R - r_i$, is enforced using the bounce-back technique.[49] The total of N charged particles consists of N_{+3} trivalent counterions and N_- monovalent co-ions, derived from the dissociated multivalent salt. The excess number of counterions is $N_c = 2\pi RL_z|\sigma|/\alpha q$, where $\alpha = 3$ is the counterion valence and q the proton charge, and it is included to preserve the overall charge neutrality of the pore−electrolyte system. In the present simulations we will fix the concentration of salt and solvent particles in the "bulk" (the center of the pore) at $\varrho_s = 0.025l_B^{-3}$ and $n_s = 4l_B^{-3}$, respectively. This corresponds to an approximately 110 mM salt concentration. The cylindrical pore is placed along the major axis of a rectangular simulation box of side length L_p, L_p, and L_z, where $L_p = 4R$. The empty space outside the cylinder is necessary in order to reduce the interaction with spurious periodic replicas produced by the 3D Ewald summation method used to account for the electrostatic interactions inside the pore.[47]

The hydrodynamic limit is obtained using the DPD method. The interactions between all of the particles are given by the following forces

$$\mathbf{F}_{ij}^{C} = \begin{cases} a_{ij}\left(1 - \frac{|\mathbf{r}_{ij}|}{r_c}\right) & \text{if } |\mathbf{r}_{ij}| \le r_c \\ 0 & \text{if } |\mathbf{r}_{ij}| > r_c \end{cases} \quad (1)$$

$$\mathbf{F}_{ij}^{D} = \begin{cases} -\gamma w_D(|\mathbf{r}_{ij}|)(\hat{\mathbf{r}}_{ij}\cdot\mathbf{v}_{ij}) & \text{if } |\mathbf{r}_{ij}| \le r_c \\ 0 & \text{if } |\mathbf{r}_{ij}| > r_c \end{cases} \quad (2)$$

$$\mathbf{F}_{ij}^{R} = \begin{cases} \frac{\Omega}{\sqrt{\Delta t}}\omega_{ij}w_R(|\mathbf{r}_{ij}|)\hat{\mathbf{r}}_{ij} & \text{if } |\mathbf{r}_{ij}| \le r_c \\ 0 & \text{if } |\mathbf{r}_{ij}| > r_c \end{cases} \quad (3)$$

where $\mathbf{r}_{ij}$ is the separation vector between particles i and j, while the cutoff radius is set to $r_c = l_B$. The softness of the collisions is controlled by the parameter a_{ij} of the conservative force in eq 1. We set $a_{ij} = 25(\beta l_B)^{-1}$ for solvent−solvent interactions and 0 for solvent−ion and ion−ion interactions. We recall that, within the DPD formalism, the soft particles do not represent individual water molecules but rather clusters of solvent molecules. The effects of temperature—randomness—are take into account by the dissipative and random forces: eqs 2 and 3, respectively. The fluctuation−dissipation theorem requires[50] that $\Omega^2 = 2\gamma K_BT$, and we set the friction parameter γ to $\gamma = 4.5(m/\beta)^{0.5}l_B^{-1}$. The weight functions are defined as $w_D(|\mathbf{r}_{ij}|) = w_R(|\mathbf{r}_{ij}|)^2$, where $w_R(|\mathbf{r}_{ij}|) = (1 - |\mathbf{r}_{ij}|/r_c)$. The force $\mathbf{F}_{ij}^{D}$ depends on the relative velocity $\mathbf{v}_{ij}$ between particle i and j, while the force $\mathbf{F}_{ij}^{R}$ depends on a uniformly distributed random number with zero mean and unit variance ω_{ij}. The step time used in the integration algorithm is set to $\Delta t = 0.005\sqrt{m\beta}/l_B$.

The charged particles are modeled using a truncated Lennard-Jones potential,[51] with $\sigma_{LJ} = 2r_i$, strength $\epsilon_{LJ} = 0.5\ (\beta)^{-1}$, and cutoff radius $r_{LJ} = 2^{1/6}\sigma_{LJ}$. The difficulty with performing simulations of Coulomb systems is that the interaction potential is long ranged, and one cannot use simple periodic boundary conditions to calculate the electrostatic energy. Instead, to obtain the correct thermodynamic limit, the system must be periodically replicated, so that each ion interacts not only with the ions inside the simulation box but also with the infinite number of periodic replicas of itself and of other ions. To efficiently sum over the replicas, one can use Ewald summation methods. However, the pseudo-one-dimensional geometry of the pore requires that the replication be performed only in one direction. On the other hand, the computationally efficient Ewald summation method results in a full 3D replication of the simulation cell. Nevertheless, it was recently shown that one can still use 3D Ewald summation for pseudo-one-dimensional systems, if a sufficiently large vacuum region is included inside the simulation cell to prevent the interaction with the spurious replicas. In addition, an extra term must be added to Ewald summation to account for the conditional convergence of the lattice sum and a preferential summation along the z-direction. The electrostatic energy of a pseudo-one-dimensional periodic system is then given by[47]

https://doi.org/10.1021/acs.langmuir.1c03475
Langmuir 2022, 38, 3817−3823

$$\beta U_e = \sum_{i=1}^{N}\sum_{j>i}^{N} q_i q_j l_B \frac{\mathrm{erfc}(\kappa_e r_{ij})}{r_{ij}} + \sum_{\mathbf{k}\neq\mathbf{0}} \frac{2\pi l_B}{V|\mathbf{k}|^2} \exp\left(-\frac{|\mathbf{k}|^2}{4\kappa_e^2}\right)[A(\mathbf{k})^2 + B(\mathbf{k})^2] + \frac{\pi l_B}{V}(M_x^2 + M_y^2 - Q_t G_x - Q_t G_y) - \frac{l_B \kappa_e}{\sqrt{\pi}} \sum_{i=1}^{N} q_i^2 \quad (4)$$

where

$$A(\mathbf{k}) = \sum_{i=1}^{N} q_i \cos(\mathbf{k}\cdot\mathbf{r})$$

$$B(\mathbf{k}) = -\sum_{i=1}^{N} q_i \sin(\mathbf{k}\cdot\mathbf{r}) \quad (5)$$

and

$$M_x = \sum_{i=1}^{N} q_i x_i,\ M_y = \sum_{i=1}^{N} q_i y_i$$

$$G_x = \sum_{i=1}^{N} q_i x_i^2,\ G_y = \sum_{i=1}^{N} q_i y_i^2 \quad (6)$$

where q_i is the charge of ion i, $\kappa_e = 5/L_z$ is the damping parameter, $V = L_p^2 L_z$ is the volume of the simulation box, while $\mathbf{k} = \left(\frac{2\pi}{L_p}n_x,\ \frac{2\pi}{L_p}n_y,\ \frac{2\pi}{L_z}n_z\right)$ are the reciprocal lattice vectors, and n's are integers. This Ewald summation method allows us to accurately and efficiently calculate the electrostatic energy of a non-neutral charged system, with the total charge $Q_t = \sum_i^N q_i$, periodically replicated in the z direction. Note that, due to Gauss's law, the uniform charge on the pore's surface does not produce any electric field in the interior of the pore and can be neglected when performing simulations. However, if this is done, the rest of the system will no longer be charge neutral. To account for the non-neutrality[47] of the pore's interior, Q_t-dependent terms appear in the Ewald summation, eq 4.

The total force that a particle i feels is the sum of the DPD, electrostatic, and Lennard-Jones contributions

$$\mathbf{F}_i = \mathbf{F}_i^{\mathrm{DPD}} + \mathbf{F}_i^{\mathrm{elec}} + \mathbf{F}_i^{\mathrm{LJ}} \quad (7)$$

where the electrostatic and Lennard-Jones forces can be obtained from the gradients of their respective energies and act only between charged particles. There is an additional force produced by the external electric field responsible for inducing the EOF. The electric field is applied in the $+z$ direction. The strength of the electric field is set to $E_z = 1(\beta e l_B)^{-1}$, so that the force on an ion i is $\mathbf{F}z = q_i E_z \hat{\mathbf{z}}$. Once the total force is obtained, the equations of motion for each particle are integrated using the velocity-Verlet algorithm.[52] A stationary flow is established after approximately 5×10^4 time steps. The samples are collected each 10 time steps to perform a statistical analysis. In total, we used 5×10^4 samples for each curve presented in the following section.

RESULTS AND DISCUSSION

We start by calculating the ion concentration profiles after a stationary flow has been established inside a nanopore of surface charge σ. In Figures 2 and 3, we present the concentration profiles of trivalent counterions and monovalent co-ions,

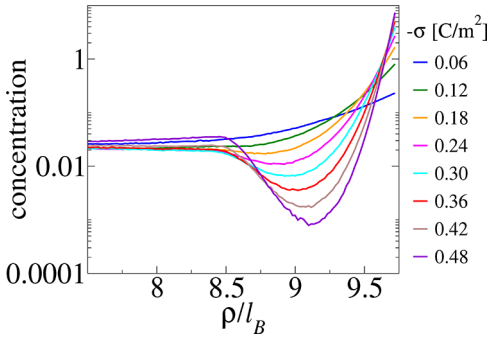

Figure 2. Concentration profiles of trivalent counterions inside cylindrical pores of various surface charge densities.

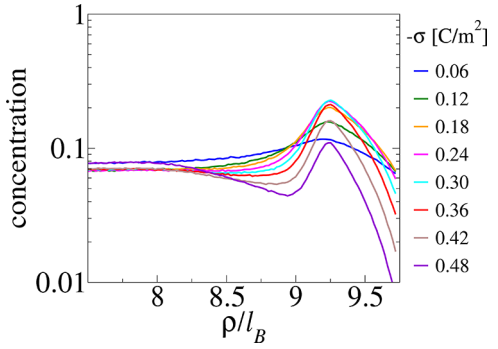

Figure 3. Concentration profiles of monovalent co-ions inside cylindrical pores of various surface charge densities.

respectively, as a function of the distance from the center of the pore, ρ. All of the results are presented in reduced units $\tilde{\varrho} = l_B^3 \varrho$.

As the surface charge of the pore is increased, we see a strong condensation of trivalent counterions onto the pore surface, resulting in the formation of a complex double layer structure. The ionic charge density, $\varrho_q(\rho) = 3q\varrho_+(\rho) - q\varrho_-(\rho)$, is shown in Figure 4, demonstrating that the local charge neutrality is established a short distance from the surface of the pore. Clearly, the body force exerted by the electric field on the fluid will act only within the range of the double layer.

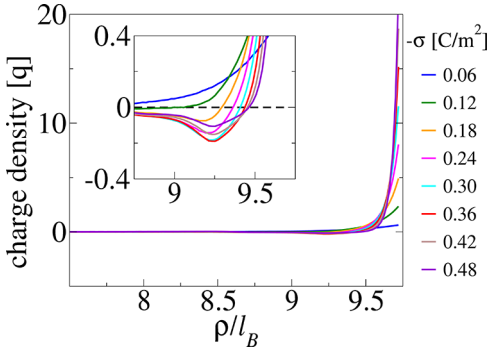

Figure 4. Charge density profiles inside pores of various surface charge densities. Inset: zoom of the region close to the pore surface; the dashed line shows zero charge density.

https://doi.org/10.1021/acs.langmuir.1c03475
Langmuir 2022, 38, 3817−3823

In Figure 5, we show the reduced fluid flow velocity profiles, $\tilde{v}_z = v_z(m\beta)^{0.5}$, inside the channel for various charge densities σ.

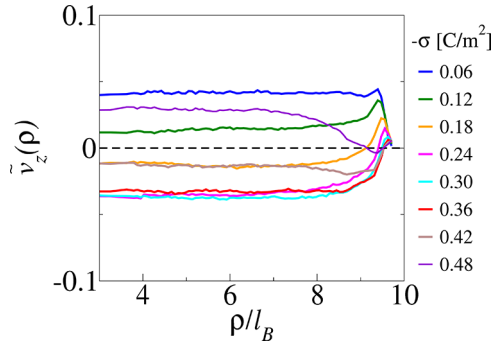

Figure 5. Fluid velocity profiles for various σ's.

We observe that, for pores of low surface charge density, the EOF flow is in the same direction as the applied electric field. This is what one expects, considering that the double layer is overall positively charged—collisions of ions with the solvent particles lead to the transfer of momentum, resulting in the EOF flow in the direction of the applied electric field. As the surface charge becomes more negative, however, we observe that the EOF flow reverses its direction. The surface charge density at which the reversal of EOF takes place is close to the experimentally measured values for the reversal of the electrophoretic of colloidal particles.[53] For even more negative σ's, the EOF inverts again; see the purple curve in Figure 5.

To obtain a more quantitative understanding of the reversals of EOF, we will appeal to continuum hydrodynamics in the low Reynolds number limit. The Stokes equation relates the fluid velocity with the body force acting on the fluid:

$$\varrho\frac{\partial \mathbf{v}}{\partial t} = \nabla P + \mathbf{E}\varrho_q + \eta\nabla^2\mathbf{v} \tag{8}$$

where $\mathbf{v}$ is the fluid velocity, ϱ is the fluid density, ϱ_q is the local charge concentration, P is the pressure, $\mathbf{E}$ is the total electric field vector, and η is the dynamic viscosity. Considering the azimuthal symmetry of the pore, we can rewrite this equation in terms of its radial and longitudinal components. For a stationary flow, the Stokes equation becomes

$$0 = \frac{\partial P}{\partial \rho}\hat{\boldsymbol{\rho}} + \frac{\partial P}{\partial z}\hat{\mathbf{z}} + E_\rho\varrho_q\hat{\boldsymbol{\rho}} + E_z\varrho_q\hat{\mathbf{z}} + \eta\nabla^2 v_z\hat{\mathbf{z}} + \eta\nabla^2 v_\rho\hat{\boldsymbol{\rho}} \tag{9}$$

Furthermore, we observe that, in the stationary state, there is no fluid flow in the radial direction, so the radial component of velocity vanishes. We then arrive at the isostatic equilibrium equation

$$\frac{\partial P}{\partial \rho} = -E_\rho\varrho_q \tag{10}$$

This equation is the same as one finds for the thermodynamic equilibrium in the absence of an applied electric field. In the present case, the only source for the osmotic pressure is the concentration gradient of salt which exists only in the radial direction. Indeed, if we use van't Hoff law for osmotic pressure, eq 10 leads to the Boltzmann distribution of ions. This suggests that, for small external electric fields, the ionic density profiles should be the same as they are in the state of thermodynamic equilibrium. Comparing the results of DPD simulations with equilibrium Monte Carlo simulations, we find this to be true, as long as the external electric field is not very large, so that osmotic pressure remains a well-defined thermodynamic quantity. We next note that ionic concentrations are invariant in the z direction. This means that osmotic pressure also does not depend on the z coordinate, and $\partial P/\partial z = 0$. The z component of eq 9 then reduces to

$$0 = E_z\varrho_q + \eta\nabla^2 v_z \tag{11}$$

The ionic charge density is related to the electrostatic potential, $\phi(\rho)$, inside the fluid by the Poisson equation:

$$\nabla^2\phi(\rho) = -\frac{4\pi}{\epsilon}[\sigma\delta(\rho - R) + \varrho_q(\rho)] \tag{12}$$

Combining eqs 11 and 12, we obtain the Smoluchowski equation for the fluid velocity inside the pore

$$v_z(\rho) = \frac{\epsilon E_z}{4\pi\eta}(\phi(\rho) - \zeta) \tag{13}$$

where we have defined the electrostatic potential at the shear plane as $\phi(\rho_s) \equiv \zeta$. The shear plane is defined as the position at which the average fluid velocity vanishes $v_z(\rho_s) = 0$. The DPD simulations allow us to calculate the fluid velocity in the center of the pore $v_z(0)$ (see Figure 5). Since the electrostatic potential at the center of the pore vanishes, we can use $v_z(0)$ and eq 13 to obtain the ζ potential

$$\tilde{\zeta} = -\frac{4\pi\tilde{\eta}\,\tilde{v}_z(0)}{\tilde{E}_z} \tag{14}$$

where $\tilde{\eta} = \eta(\beta/m)^{0.5}l_B^2$ and $\tilde{E}_z = \beta q l_B E_z$. The reduced dynamic viscosity for the present model parameters was calculated using a separate DPD simulation of Poiseuille flow,[54] resulting in $\tilde{\eta} = 1.13$. The reduced ζ potential, $\tilde{\zeta} = \beta q\zeta$, is shown in Figure 6 (blue circles) as a function of pore surface charge density.

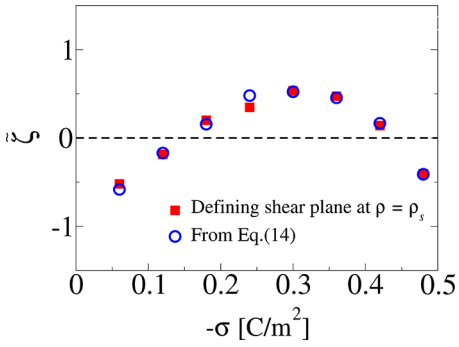

Figure 6. ζ potential as a function of the surface charge density σ. Blue circles were obtained using eq 14, while the red squares correspond to the electrostatic potential calculated at the location of the shear surface, $\phi(\rho_s)$.

To locate the position of the shear plane, we need to calculate the mean electrostatic potential, $\phi(\rho)$, inside the pore. The mean electric field in the stationary state can be calculated from the ionic charge distribution using Gauss's law:

$$E_\rho(\rho) = \frac{4\pi}{\epsilon\rho}\int_0^\rho d\rho'\,\rho'\varrho_q(\rho') \tag{15}$$

The electrostatic potential is then

https://doi.org/10.1021/acs.langmuir.1c03475
Langmuir 2022, 38, 3817−3823

$$\phi(\rho) = -\frac{4\pi}{\epsilon}\int_0^{\rho} d\rho' \frac{1}{r'}\int_0^{\rho'} d\rho'' \rho'' \varrho_q(\rho'') \tag{16}$$

Performing the integration by parts, we obtain

$$\phi(\rho) = \frac{4\pi}{\epsilon}\int_0^{\rho} d\rho' \rho' \log\left(\frac{\rho'}{\rho}\right)\varrho_q(\rho') \tag{17}$$

In Figure 7, we show the reduced electrostatic potential inside the cylinder, $\tilde{\phi} = \beta q \phi$, for various pore surface charge densities.

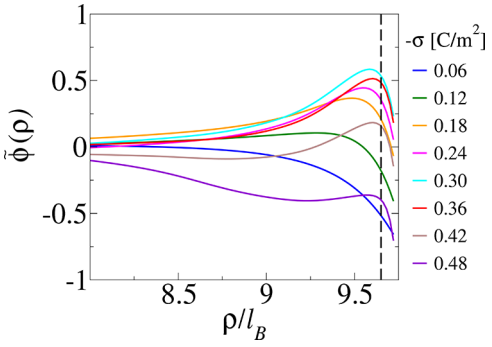

Figure 7. Electrostatic potentials, eq 17. The dashed line indicates the shear plane, $\tilde{\rho}_s = \tilde{R} - \tilde{r}_i - 0.1$.

We locate the shear plane at the position where $\phi(\rho_s)$ agrees with the ζ potential calculated using eq 14 for $\sigma = -0.12$ C/m^2. This yields $\tilde{\rho} = \tilde{\rho}_s = \tilde{R} - \tilde{r}_i - 0.1$; see the dashed line in Figure 7. In Figure 6, we see that the same location of the shear plane leads to correct values of ζ potential for other pore surface charge densities. Note that the shear surface ρ_s is shifted from the contact surface, $R - r_i$, by $0.1l_B$. We observe an identical shift for other model parameters, such as monovalent electrolyte, ions of different radii, and other salt concentrations. This suggests that the location of the shear plane is a property of the pure DPD fluid and is only very weakly influenced by the electrolyte. To confirm this, in Figure 8, we plot the velocity profile of a pure DPD fluid in which particles move under the action of a constant gravitational field. Indeed, we observe that the fluid velocity vanishes at a distance of about $0.1l_b$ from the contact surface, at which the bounce-back no-slip boundary condition is enforced. The presence of a stagnated fluid layer of width $0.1l_b$ away from the contact surface helps us to understand the reversal of the

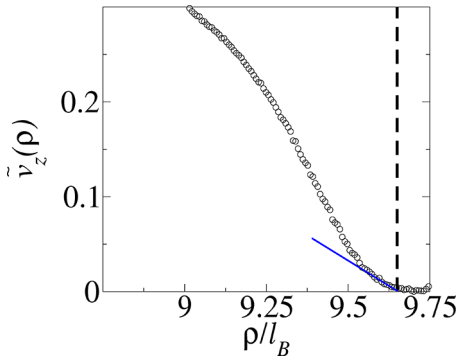

Figure 8. Pure-fluid DPD simulation (without ions) for a pressure gradient flow. The dashed line indicates the location of the shear plane, $\tilde{\rho}_s = \tilde{R} - \tilde{r}_i - 0.1$. The blue line shows a linear extrapolation of the low velocity region to zero.

EOF flow observed earlier. Strong electrostatic correlations[55] result in the reversal of the pore surface charge—more trivalent ions crowd into the stagnation layer than is necessary to completely neutralize the pore charge. Within the stagnation layer, these ions have zero velocity with respect to the surface. The rest of the double layer will then have a net negative charge, resulting in the reversal of the EOF. If the pore surface charge increased even further, i.e., made even more negative, hardcore repulsion between the counterions will limit the number of trivalent ions that can be condensed within the stagnation zone, preventing the charge reversal from taking place inside this region. Thus, for very negative pores, a reversal of EOF will not happen. Indeed, this is what we observe in the simulations (see Figure 5) showing that, for large negative σ's, the EOF is, once again, in the direction of the applied electric field.

The reversal of EOF is not possible for monovalent ions in water. For 1:1 electrolyte, the correlations between counterions are negligible, and charge reversal cannot take place.[55] This is indeed confirmed by our DPD simulations, showing that for 1:1 electrolyte there is no reversal of EOF.

To more precisely explore the EOF through a cylindrical nanopore, we calculate the volumetric flow rate (VFR) defined as

$$Q = 2\pi\int_0^R \rho v_z(\rho)\, d\rho \tag{18}$$

The reduced VFR, $\tilde{Q} = (m\beta)^{0.5} l_B^{-2} Q$, is shown as a function of σ in Figure 9, red squares.

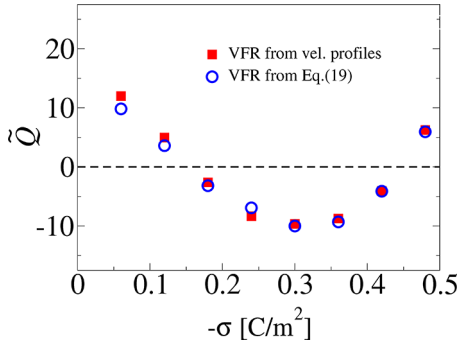

Figure 9. Volumetric flow rate as a function of charge density. Red squares represent data obtained using fluid velocity in DPD (eq 18), while the blue circles are calculated using the electrostatic potential and eq 19.

The VFR can also be obtained in terms of the mean electrostatic potential. Inserting eq 13 into eq 18, we obtain

$$\tilde{Q} = \frac{\tilde{E}_z}{2\tilde{\eta}}\int_0^{\tilde{\rho}_s} \tilde{\rho}(\tilde{\phi}(\rho) - \tilde{\zeta})\, d\tilde{\rho} \tag{19}$$

The comparisons of VFRs calculated using fluid velocity in DPD with results obtained using eq 19 are shown in Figure 9. We conclude that the Smoluchowski equations remain very accurate even for multivalent electrolytes. Therefore, if the mean electrostatic potential is known, e.g., from an independent Monte Carlo simulation, and *if* the position of the shear plane is also known, then we can calculate the VFR using equilibrium statistical mechanics. There does not appear to be a way to obtain the position of the shear plane from purely equilibrium considerations. However, the fact that ρ_s depends only on the solvent permits us to locate the position of the shear surface by

https://doi.org/10.1021/acs.langmuir.1c03475
Langmuir 2022, 38, 3817−3823

performing a single pure-fluid DPD simulation. Once ρ_s is located using linear extrapolation (see Figure 8), we can calculate the whole EOF using purely equilibrium statistical mechanics combined with the Smoluchowski equation (eq 13).

Finally, it is interesting to calculate the electric current flowing through the nanopore:

$$I = \frac{q}{L_z}\left\langle \sum_{i=1}^{N} q_i v_{zi} \right\rangle_{\text{samples}} \tag{20}$$

where v_{zi} is the z component of velocity of particle i. The conductance is defined as $G = I/V$, where $V = -E_z L_z$. In Figure 10, we plot the reduced conductance $\tilde{G} = (m\beta)^{0.5}\epsilon^{-1}G$ for

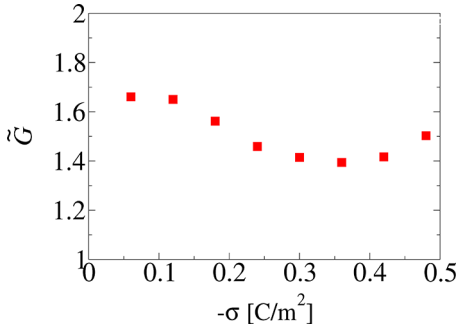

Figure 10. Conductance as a function of surface charge density.

various surface charge densities. We see that $\tilde{G}$ is only weakly dependent on the pore surface charge density. This is not very surprising since both the flow of cations *in the direction* of the applied electric field and the flow of anions in the *opposite direction* to the electric field produce positive contributions to the electric current. Unlike the EOF, which is intrinsically a surface phenomenon, the electric current inside the pore is dominated by the bulk motion of ions. This makes it only weakly dependent on the overall fluid velocity induced by the EOF. Nevertheless, we see an appearance of an inflection point in the conductance at the value of the surface charge density at which the reversal of EOF takes place.

CONCLUSIONS

We have studied the electroosmotic flow in charged cylindrical nanopores containing multivalent electrolyte. To efficiently explore the hydrodynamic limit of the electroosmotic flow, we have used dissipative particle dynamics simulations. The electrostatic interactions were treated using 3D Ewald summation, corrected for the pseudo-one-dimensional geometry of the pore. We observe that, for sufficiently large surface charge density, condensation of multivalent counterions leads to the charge reversal of a pore's surface. This results in the reversal of electroosmotic flow. Our simulations show that the Smoluchowski equation is able to account *quantitatively* for the electroosmotic flow, if the shear surface is shifted away from the contact surface position. Indeed, we find that the location of the shear surface can be obtained from the simulation of a pure DPD fluid, without any ions. Finally, we observe that both ζ potential and the volumetric flow rate are nonmonotonic functions of the pore surface charge density—indicating the important role played by steric effects for strongly charged nanopores.

AUTHOR INFORMATION

Corresponding Authors

Igor M. Telles − *Instituto de Física, Universidade Federal do Rio Grande do Sul, Porto Alegre, Rio Grande do Sul CEP 91501-970, Brazil*; Email: igor.morais@ufrgs.br

Yan Levin − *Instituto de Física, Universidade Federal do Rio Grande do Sul, Porto Alegre, Rio Grande do Sul CEP 91501-970, Brazil*; orcid.org/0000-0002-0636-7300; Email: levin@if.ufrgs.br

Alexandre P. dos Santos − *Instituto de Física, Universidade Federal do Rio Grande do Sul, Porto Alegre, Rio Grande do Sul CEP 91501-970, Brazil*; orcid.org/0000-0002-5965-3992; Email: alexandre.pereira@ufrgs.br

Complete contact information is available at: https://pubs.acs.org/10.1021/acs.langmuir.1c03475

Notes

The authors declare no competing financial interest.

ACKNOWLEDGMENTS

This work was supported by CAPES, CNPq, INCT-FCx, and FAPERGS.

REFERENCES

(1) Siwy, Z. S. Ion-Current Rectification in Nanopores and Nanotubes with Broken Symmetry. *Adv. Funct. Mater.* **2006**, *16*, 735−746.

(2) Zhu, Z.; Wang, D.; Tian, Y.; Jiang, L. Ion/Molecule Transportation in Nanopores and Nanochannels: From Critical Principles to Diverse Functions. *J. A. Chem. Soc.* **2019**, *141*, 8658−8669.

(3) Merlet, C.; Limmer, D. T.; Salanne, M.; van Roij, R.; Madden, P. A.; Chandler, D.; Rotenberg, B. The Electric Double Layer Has a Life of Its Own. *J. Phys. Chem. C* **2014**, *118*, 18291−18298.

(4) Xiao, K.; Jiang, L.; Antonietti, M. Ion Transport in Nanofluidic Devices for Energy Harvesting. *Joule* **2019**, *3*, 2364−2380.

(5) Xiao, K.; Chen, L.; Chen, R.; Heil, T.; Cruz, D.; Fan, F.; Wen, L.; Jiang, L.; Antonietti, M. Artificial light-driven ion pump for photoelectric energy conversion. *Nat. Commun.* **2019**, *10*, 74.

(6) Feng, G.; Cummings, P. T. Supercapacitor Capacitance Exhibits Oscillatory Behavior as a Function of Nanopore Size. *J. Phys. Chem. Lett.* **2011**, *2*, 2859−2864.

(7) Jiang, D.-e.; Jin, Z.; Henderson, D.; Wu, J. Solvent Effect on the Pore-Size Dependence of an Organic Electrolyte Supercapacitor. *J. Phys. Chem. Lett.* **2012**, *3*, 1727−1731.

(8) Maier, J. Nanoionics: Ion Transport and Electrochemical Storage in Confined Systems. *Nat. Mater.* **2005**, *4*, 805−15.

(9) Ramírez, P.; Gómez, V.; Cervera, J.; Schiedt, B.; Mafé, S. Ion transport and selectivity in nanopores with spatially inhomogeneous fixed charge distributions. *J. Chem. Phys.* **2007**, *126*, 194703.

(10) Duong-Hong, D.; Han, J.; Wang, J.-S.; Hadjiconstantinou, N.; Chen, Y.; Liu, G. R. Realistic simulations of combined DNA electrophoretic flow and EOF in nano-fluidic devices. *Electrophoresis* **2008**, *29*, 4880−6.

(11) Marbach, S.; Bocquet, L. Osmosis, from molecular insights to large-scale applications. *Chem. Soc. Rev.* **2019**, *48*, 3102−3144.

(12) Guo, W.; Cao, L.; Xia, J.; Nie, F.-Q.; Ma, W.; Xue, J.; Song, Y.; Zhu, D.; Wang, Y.; Jiang, L. Energy Harvesting with Single-Ion-Selective Nanopores: A Concentration-Gradient-Driven Nanofluidic Power Source. *Adv. Funct. Mater.* **2010**, *20*, 1339−1344.

(13) Modi, N.; Winterhalter, M.; Kleinekathöfer, U. Computational modeling of ion transport through nanopores. *Nanoscale* **2012**, *4*, 6166−6180.

(14) Breitsprecher, K.; Janssen, M.; Srimuk, P.; Mehdi, B. L.; Presser, V.; Holm, C.; Kondrat, S. How to speed up ion transport in nanopores. *Nat. Commun.* **2020**, *11*, 6085.

(15) Zheng, Z.; Hansford, D. J.; Conlisk, A. T. Effect of multivalent ions on electroosmotic flow in micro- and nanochannels. *Electrophoresis* **2003**, *24*, 3006−3017.
(16) van der Heyden, F. H. J.; Stein, D.; Besteman, K.; Lemay, S. G.; Dekker, C. Charge Inversion at High Ionic Strength Studied by Streaming Currents. *Phys. Rev. Lett.* **2006**, *96*, 224502.
(17) Perez Sirkin, Y. A.; Tagliazucchi, M.; Szleifer, I. Transport in nanopores and nanochannels: some fundamental challenges and nature-inspired solutions. *Mater. Today Adv.* **2020**, *5*, 100047.
(18) Rathore, A.; Horváth, C. Capillary electrochromatography: theories on electroosmotic flow in porous media. *J. Chromatogr. A* **1997**, *781*, 185−195.
(19) Garcia, A. L.; Ista, L. K.; Petsev, D. N.; O'Brien, M. J.; Bisong, P.; Mammoli, A. A.; Brueck, S. R. J.; López, G. P. Electrokinetic molecular separation in nanoscale fluidic channels. *Lab Chip* **2005**, *5*, 1271−1276.
(20) Petersen, B.; Roa, R.; Dzubiella, J.; Kanduč, M. Ionic structure around polarizable metal nanoparticles in aqueous electrolytes. *Soft Matter* **2018**, *14*, 4053−4063.
(21) dos Santos, A. P.; Netz, R. R. Dielectric boundary effects on the interaction between planar charged surfaces with counterions only. *J. Chem. Phys.* **2018**, *148*, 164103.
(22) Angelova, A.; Angelov, B.; Lesieur, S.; Mutafchieva, R.; Ollivon, M.; Bourgaux, C.; Willumeit, R.; Couvreur, P. Dynamic control of nanofluidic channels in protein drug delivery vehicles. *J. Drug Delivery Sci. Tec.* **2008**, *18*, 41−45.
(23) Moeendarbary, E.; Ng, T.; Pan, H.; Lam, K. Migration of DNA molecules through entropic trap arrays: A dissipative particle dynamics study. *Microfluid. Nanofluid.* **2010**, *8*, 243−254.
(24) Hatlo, M. M.; Panja, D.; van Roij, R. Translocation of DNA Molecules through Nanopores with Salt Gradients: The Role of Osmotic Flow. *Phys. Rev. Lett.* **2011**, *107*, 068101.
(25) Khodabandehloo, A.; Chen, D. D. Y. Electroosmotic Flow Dispersion of Large Molecules in Electrokinetic Migration. *Anal. Chem.* **2017**, *89*, 7823−7827.
(26) Anastos, N.; Barnett, N. W.; Lewis, S. W. Capillary electrophoresis for forensic drug analysis: A review. *Talanta* **2005**, *67*, 269−279.
(27) Bartzis, V.; Sarris, I. E. Electric field distribution and diffuse layer thickness study due to salt ion movement in water desalination. *Desalination* **2020**, *490*, 114549.
(28) Probstein, R. F.; Hicks, R. E. Removal of Contaminants from Soils by Electric Fields. *Science* **1993**, *260*, 498−503.
(29) Martin, L.; Alizadeh, V.; Meegoda, J. Electro-osmosis treatment techniques and their effect on dewatering of soils, sediments, and sludge: A review. *Soils Found.D* **2019**, *59*, 407−418.
(30) Harnett, C. K.; Templeton, J.; Dunphy-Guzman, K. A.; Senousy, Y. M.; Kanouff, M. P. Model based design of a microfluidic mixer driven by induced charge electroosmosis. *Lab Chip* **2008**, *8*, 565−572.
(31) Wang, X.; Cheng, C.; Wang, S.; Liu, S. Electroosmotic pumps and their applications in microfluidic systems. *Microfluid. Nanofluid.* **2009**, *6*, 145.
(32) Kirby, B. *Micro- and Nanoscale Fluid Mechanics: Transport in Microfluidic Devices*; Cambridge University Press, 2010.
(33) Leong, I. W.; Tsutsui, M.; Murayama, S.; He, Y.; Taniguchi, M. Electroosmosis-Driven Nanofluidic Diodes. *J. Phys. Chem. B* **2020**, *124*, 7086−7092.
(34) Koranlou, A.; Ashrafizadeh, S. N.; Sadeghi, A. Enhanced electrokinetic energy harvesting from soft nanochannels by the inclusion of ionic size. *J. Phys. D Appl. Phys.* **2019**, *52*, 155502.
(35) Brown, W.; Kvetny, M.; Yang, R.; Wang, G. Higher Ion Selectivity with Lower Energy Usage Promoted by Electro-osmotic Flow in the Transport through Conical Nanopores. *J. Phys. Chem. C* **2021**, *125*, 3269−3276.
(36) Arima, A.; Tsutsui, M.; Washio, T.; Baba, Y.; Kawai, T. Solid-State Nanopore Platform Integrated with Machine Learning for Digital Diagnosis of Virus Infection. *Anal. Chem.* **2021**, *93*, 215−227.
(37) Qiao, R.; Aluru, N. R. Charge Inversion and Flow Reversal in a Nanochannel Electro-osmotic Flow. *Phys. Rev. Lett.* **2004**, *92*, 198301.
(38) Hartkamp, R.; Siboulet, B.; Dufrêche, J.-F.; Coasne, B. Ion-specific adsorption and electroosmosis in charged amorphous porous silica. *Phys. Chem. Chem. Phys.* **2015**, *17*, 24683−24695.
(39) Předota, M.; Machesky, M. L.; Wesolowski, D. J. Molecular Origins of the Zeta Potential. *Langmuir* **2016**, *32*, 10189−10198.
(40) Celebi, A. T.; Cetin, B.; Beskok, A. Molecular and Continuum Perspectives on Intermediate and Flow Reversal Regimes in Electro-osmotic Transport. *J. Phys. Chem. C* **2019**, *123*, 14024−14035.
(41) Lozada-Cassou, M.; Saavedra-Barrera, R.; Henderson, D. The application of the hypernetted chain approximation to the electrical double layer: Comparison with Monte Carlo results for symmetric salts. *J. Chem. Phys.* **1982**, *77*, 5150−5156.
(42) Deserno, M.; Jiménez-Ángeles, F.; Holm, C.; Lozada-Cassou, M. Overcharging of DNA in the Presence of Salt: Theory and Simulation. *J. Phys. Chem. B* **2001**, *105*, 10983.
(43) Diehl, A.; Levin, Y. Smoluchowski equation and the colloidal charge reversal. *J. Chem. Phys.* **2006**, *125*, 054902.
(44) Lyklema, J.; Golub, T. Electrical double layer on silver iodide and overcharging in the presence of hydrolyzable cations. *Croat. Chem. Acta* **2007**, *80*, 303−311.
(45) Uematsu, Y. Electrification of water interface. *J. Phys.: Condens. Matter* **2021**, *33*, 423001.
(46) Groot, R. D.; Warren, P. B. Dissipative particle dynamics: Bridging the gap between atomistic and mesoscopic simulation. *J. Chem. Phys.* **1997**, *107*, 4423−4435.
(47) Telles, I. M.; Bombardelli, R. K.; dos Santos, A. P.; Levin, Y. Simulations of electroosmotic flow in charged nanopores using Dissipative Particle Dynamics with Ewald summation. *J. Mol. Liquid.* **2021**, *336*, 116263.
(48) Bombardelli, R. K.; Telles, I. M.; dos Santos, A. P.; Levin, Y. Electroosmotic Flow in Polarizable Charged Cylindrical Nanopores. *J. Phys. Chem. B* **2021**, *125*, 11091−11098.
(49) Pivkin, I.; Karniadakis, G. A new method to impose no-slip boundary conditions in dissipative particle dynamics. *J. Comput. Phys.* **2005**, *207*, 114−128.
(50) Español, P.; Warren, P. Statistical Mechanics of Dissipative Particle Dynamics. *Europhys. Lett.* **1995**, *30*, 191−196.
(51) Ahmed, A.; Sadus, R. Phase diagram of the Weeks-Chandler-Andersen potential from very low to high temperatures and pressures. *Phys. Rev. E* **2009**, *80*, 061101.
(52) Allen, M. P.; Tildesley, D. J. *Computer Simulations of Liquids*; Oxford University Press: Oxford, 1987.
(53) Trefalt, G.; Behrens, S. H.; Borkovec, M. Charge Regulation in the Electrical Double Layer: Ion Adsorption and Surface Interactions. *Langmuir* **2016**, *32*, 380−400.
(54) Smiatek, J.; Allen, M.; Schmid, F. Tunable-slip boundaries for coarse-grained simulations of fluid flow. *Eur. Phys. J. E* **2008**, *26*, 115−22.
(55) Levin, Y. Electrostatic Correlations: from Plasma to Biology. *Rep. Prog. Phys.* **2002**, *65*, 1577−1632.

https://doi.org/10.1021/acs.langmuir.1c03475
Langmuir 2022, 38, 3817−3823